Selective laser melting of AlCu-TiB$_2$ alloy using pulsed wave laser emission mode: processability, microstructure and mechanical properties

Carlo Alberto Biffi [a], Paola Bassani [a], Jacopo Fiocchi [a,*], Mihaela Albu [b], Ausonio Tuissi [a]

[a] CNR ICMATE, National Research Council, Institute of Condensed Matter Chemistry and Technologies for Energy, Unit of Lecco, CNR ICMATE, Via Previati 1/e, 23900 Lecco, Italy
[b] Graz Centre for Electron Microscopy, Steyrergasse 17, 8010 Graz, Austria

HIGHLIGHTS

- The selective laser melting processability of an AlCu alloy with in-situ TiB$_2$ nano-particles was explored and analysed.
- Multi-scale microstructural analysis revealed fine equiaxed grains and several micrometric and nanometric secondary phases.
- Mechanical behaviour was characterized by low strain hardening and evident jerky flow.

GRAPHICAL ABSTRACT
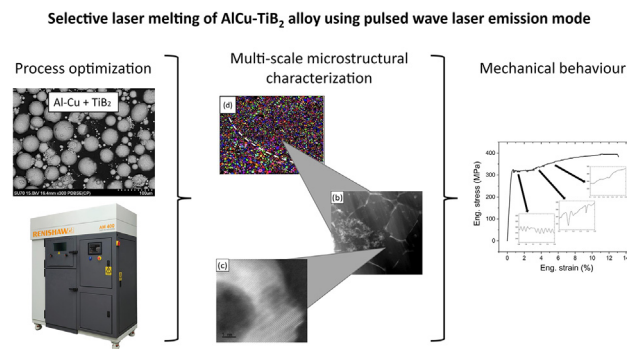
ARTICLE INFO

ABSTRACT

The present work explores the processability of an advanced aluminum alloy, namely AlCu-TiB$_2$, by selective laser melting (SLM), and the correlation between microstructure and mechanical properties of as built specimens. The principal process parameters of the laser emission in pulsed wave (PW) mode, namely laser power and exposure time, were varied to achieve full density parts starting from prealloyed powders. Detailed analysis of defects in the highest relative density conditions was performed thzrough X-ray computed tomography. It was found that the highest relative density, up to 99.5%, was achieved at a laser energy density of 82 J/mm^3. Microstructure of as-built specimens was analyzed through scanning electron microscopy, coupled with EDX and EBSD analyses, and transmission electron microscopy. The as-built microstructure was considerably uniform, and characterized by fine equiaxed grains, decorated with micrometric and nanometric second phases and an even distribution of reinforcing TiB$_2$ particles; no epitaxial grain growth was observed. Finally, tensile behaviour of the as-built specimens indicates a yield and ultimate tensile stress of 325 MPa and 395 MPa, respectively, combined with an elongation of 13%. The low work hardening rate and jerky flow characterizing plastic deformation are analyzed and discussed.

---

* Corresponding author.
  E-mail address: jacopo.fiocchi@icmate.cnr.it (J. Fiocchi).

1. Introduction

Selective laser melting (SLM) is a well-known additive manufacturing process, based on a layer by layer approach: metallic powders, deposited in a uniform bed, are melted by a high power laser beam according to a specific path [1]. The high power transferred by the laser to the melt pool and its small size locally produce an extremely high energy density, for short time, which leads to high heating and cooling rates [2]. In this respect, SLM may be considered as a rapid solidification technique and, as such, it is known to induce peculiar microstructures in the processed materials, which is characterized by refined grain size, formation of supersaturated solid solutions and presence of residual stresses. After years of continuous research and industrial development, selective laser melting of aluminium alloys can be rightfully considered as a relatively mature reality [3]. Most of the scientific studies, as well as the majority of the industrial production, have focused their attention on alloys belonging to the Al – Si system, because of their good castability [4]. This situation has been determined by the large availability of powders and relative ease of production, deriving from low melting temperature, low shrinkage and good fluidity. Nevertheless, such alloys, i.e. mainly AlSi12, AlSi7Mg, AlSi10Mg and AlSi9Cu3, display mechanical properties which cannot compete with the performances of conventionally produced high-strength aluminium alloys such as the ones belonging to the 2xxx and 7xxx series alloys, commonly produced by plastic deformation. The SLM-based production of parts from such alloys proved to be difficult due to large solidification range and shrinkage, that resulted in solidification cracking [5,6]. Recent works on SLM production strategies and advanced microstructure investigations have been presented to highlight solidification effects on mechanical properties of the as-built and thermally treated parts [7–9].

Other SLM production routes involving in situ alloying with or without the addition of nanoparticles have also been investigated by various research groups. In particular, two strategies have been pursued: in one case alloying elements (mainly Si) have been added in order to obtain an eutectic phase able to limit solidification cracking [10]; in the second case inoculants have been added to modify solidification microstructure and to obtain fine equiaxed grains. These inoculants may come under the form of ex-situ nanometric particles [11,12] or as in-situ precipitates forming upon solidification [13]. The latter type of inoculants includes Al_3Sc precipitates [14], commonly present in Al-Mg-Sc-Zr alloys, and TiB_2 particles, which were also used as ex-situ additions in an Al-Cu-Mg-Si alloy [15] and a modified ENAW 2618 alloy [16]. A further advantage of using inoculants lies in their ability of acting as reinforcing phase, thus improving the alloy mechanical properties. The addition of inoculants to materials for laser processes has potentially unknown effects, as differences occurs with respect to the conventionally cast materials. In fact, the cooling rates in SLM are typically much higher than in conventional casting processes (up to 10^4–10^6 °C/s), hence the nucleation effect may be mitigated by predominant effect of high cooling rate [17].

Recently, an aluminium powder, based on the addition of Ti and B to an Al-Cu-Mg-Ag alloy, has become commercially available under the A205 denomination. The presence of Cu and Mg in the base alloy allows to enhance mechanical properties through precipitation hardening. Further additions of Ag, Ti and B (TiB_2 formation thereof) impart also enhanced resistance at high temperature for aluminiumaluminum alloys: the use of such material, due to increased alloying costs, is intended for highly demanding applications [18–20].

The possibility of obtaining a sound component directly by SLM makes the exploration of such alloy extremely interesting: the SLM process, despite higher initial costs of powders, can more efficiently employ the feedstock materials, producing less scrap, and enhanced design solution can be explored for highly demanding applications. Moreover, as the material possibly does not require high temperature treatments, due to enhanced solubilisation effect promoted by high cooling rates already observed in other aluminium alloys [21,22], the refined

Table 1
Nominal chemical composition (weight.%) of the AlCu-TiB₂ powder.

Si	Mg	Cu	Ag	B	Ti	Fe	Mn	Ni	Pb	Al
0.1	0.29	4.7	0.7	1.46	3.51	0.02	<0.05	<0.05	<0.05	Bal.

microstructure generally obtained by SLM process can be preserved, and it can further contribute to increased mechanical performances.

Another interesting technological aspect to be considered is the sensibility of aluminium alloys to be processed using continuous wave (CW) and pulsed wave (PW) laser emission mode [23]. The heat transfer experienced by the alloy can be shifted to different thermal cycles induced by the laser scanning: this can promote specific microstructural features, which require high resolution transmission electron microscopy investigations to be revealed.

In the present work the processability of PW laser emission mode SLM of AlCu-TiB₂ alloy was investigated and a deep characterization of the obtained microstructure was carried out. In details, the effect of laser power and exposure time on the relative density was highlighted. Micro CT Xray was used to support defect mapping. Thereafter, SEM, EDS, EBSD and TEM analysis were performed on as-built samples and the mechanical response of the optimal SLM condition was measured.

2. Materials and experimental procedure

Samples were SLMed from gas-atomized powder of AlCu-TiB₂ alloy (commercial denomination is A205, supplied by LPW Technology, Ltd.), which exhibited the nominal composition reported in Table 1. Nominal powder size distribution was characterized by D10 equal to 20 μm, and D90 of 63 μm. As shown in Fig. 1, the shape is mainly spherical, displaying some satellites and irregularities.

A Renishaw AM400 machine, based on a 400-W pulsed wave fiber laser and equipped with a reduced build volume (75 mm × 75 mm × 50 mm), was used to produce AlSi10Mg samples built on an AlSi10Mg platform.

In the experiments, laser power and exposure time were varied according to a full factorial design, whereas the other process parameters were kept unchanged, as listed in Table 2. Each scanning layer was rotated by 67° with respect to the previous one, and the scheme was repeated every 180 layers. During the SLM process, the O₂ content was below 100 ppm.

Built samples were small prisms (8 mm × 8 mm × 10 mm) for density measurements and metallographic analyses and 2 mm – thick laminas, lying in the xz plane, for tensile testing, as depicted by the schematic in Fig. 1b. The reader is also referred to the reference directions in Fig. 1b for understanding the spatial orientation of analysed samples throughout the present paper: basically, xy surfaces are parallel to the building platform and perpendicular to the building direction; conversely, xz surfaces are perpendicular to the building platform and parallel to the building direction.

Part density was measured by Archimedes's principle using a Gibertini E50S2 precision digital balance and considering a full density of 2.85 g/cm³, as reported in the technical datasheet of the powder.

X-ray Computed Tomography (CT) was performed on a prismatic portion of a sample, using a XTH225 –ST system, from Nikon, having an X-ray Gun of 225 kV and a 16 bit flat panel Varex 4343CT as detector, to highlight the defects within the entire volume of the sample. The following settings were used for the measurements: (i) voltage of 144 kV; (ii) 8 μm as resolution of the detector; (iii) 105 min as scanning time.

Thermal analysis was carried out on small specimens (about 20 mg in weight) for detecting the melting point and the corresponding latent heat of melting; a differential thermal analyser (mod. SDT Q600 from TA Instruments) was used with heating rate of 10 °C/min from 30 °C up to 800 °C.
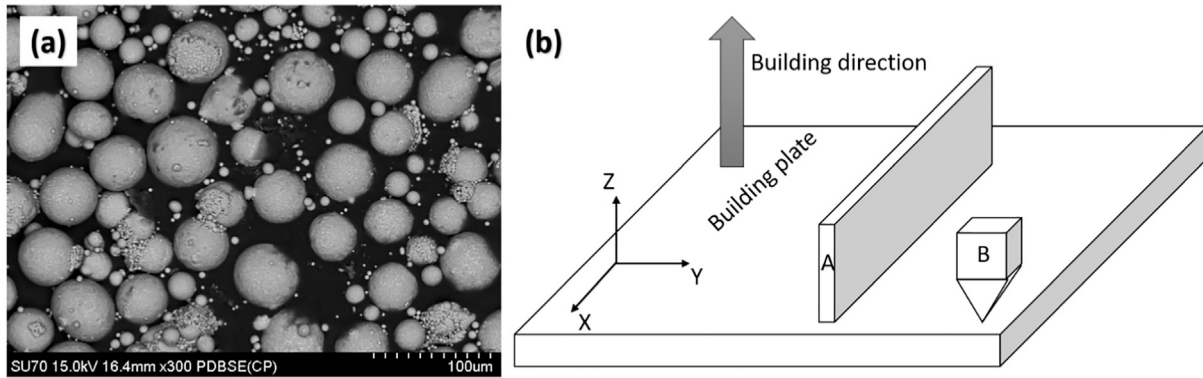
Fig. 1. (a) SEM image of the AlCu-TiB$_2$ powder; (b) schematic depicting the built samples.

Scanning electron microscopy investigations were performed with a FEG-SEM (SU70, by Hitachi), equipped with backscattered electron detector, conventional and in-lens secondary electron detectors. For the analytical and crystallographic investigations of the grains and grain boundaries, a dispersive X-ray spectrometer and EBSD technique were used (Ultradry EDX detector, Quasor detector and Pathfinder analysis system from Thermo Fisher). Specimens were embedded in conductive resin and polished first with emery paper and diamond pasts, and finally with colloidal silica. XRD analyses for phase identification was performed (Panalytical X'Pert Pro, using Cu Kα radiation) on the xz surface of the sample in the 2theta range of 20°–120°. TEM High resolution analyses were carried out on thinned specimens. The as-built sample was cut in the xz plane (along the building direction), polished and dimpled down to a thickness of about 50–80 μm and subsequently thinned using a cooled stage Ar-ion milling system (Gatan - PIPS II). The thin foil was exposed to 4 kV Ar ion beams (incident angles of 10°) at a temperature of −170 °C until perforating the sample. High-resolution STEM investigations were carried out by using the FEI Titan3 G2 60–300 at 300 kV beam voltage. The HR-STEM images were recorded with annular dark field (ADF) and high angle annular dark field (HAADF) detectors, while the chemical composition of individual grains and particles was detected by energy dispersive X-ray spectroscopy (EDXS) and electron energy loss spectroscopy (EELS). The microscope is equipped with a FEI Super-X detector (Chemi-STEM technology) for EDXS and with a Dual EELS Quantum Gatan Imaging Filter (GIF) for electron energy loss analysis. The micrographs and EELS spectra were processed using Gatan's Digital Micrograph Software.

Tensile tests were performed according to the E8/E8M-11 ASTM standard on sub-sized specimen with a crosshead speed of 0.5 mm/min (3.3 10^{-4} s^{-1}) using an MTS 2/M universal testing machine at room temperature. Three samples in the as-built condition, built with the longer side parallel to the building platform (see Fig. 1b), were tested. The specimens were machined by wire electrical discharge cutting to dogbone shape and the surface was then finished with 600 grit SiC abrasive paper grinding: this allowed to remove possible

contributions from the near-surface material, which is known to possibly behave differently because of the different thermal history experienced during the building process.

3. Results and discussion

3.1. SLM processability

The energy provided by the laser to the powder bed during SLM processing may be described by a volumetric energy density (Ψ), whose expression for a PW laser [22], is reported in the following:

$$\Psi = \frac{P \cdot t_{ex_P}}{d_p \cdot d_h \cdot s} \tag{1}$$

where P is the laser power, t_{exp} is the exposure time, d_p is the point distance, d_h is the hatch spacing, and s is the layer thickness.

An appropriate feasibility window was identified by varying the main process parameters (power and exposure time), which are representative of the PW emission mode, in order to maximize the relative density. Fig. 2a reports the evolution of the relative density of the specimens produced with the laser power and exposure time values, listed in Table 2, while Fig. 2b shows the effect of the energy density, Ψ, on the densification of the AlCu-TiB$_2$ alloy.

The histogram shown in Fig. 2a indicates that the lower value of laser power allows to obtain higher relative density, while the increase of interaction time causes a better densification. These results highlight that laser power and exposure time have an opposite effect of the relative density of the AlCu-TiB$_2$ powder processed using a PW laser emission mode, even though both these parameters are directly proportional to the energy density Ψ.

Specimens produced with different energy densities exhibit diverse shape, size and distribution of defects, as the prevalent defect formation mechanism [23,24] varies according to energy density. These defects can be associated to different regions of a processability map, as qualitatively shown in the schematic of Fig. 3. Literature reports that different types of defects are caused by a combination of different phenomena, such as key-hole, shrinkage, balling and lack of fusion [25,26]. The most common defects, which can be found in SLMed parts, are irregular porosities, due to lack of fusion, and spherical pores, due to gas entrapment (see pictures in Fig. 4).

The evolution of relative density as a function of Ψ, depicted in Fig. 2b, presents the typical trend for SLMed specimens in different alloys [27–29]. At low energy density, incomplete melting occurs, due to the energy being insufficient for the fusion of the initial powder: irregular defects of some tenths of microns in size are induced in large number, as shown in Fig. 4a. An increase of the energy density can promote a rapid increase of the relative density up to its maximum value (see Fig. 4b). A further increase of the energy density induces a soft density

Table 2
Varied and fixed process parameters.

Varied parameters	Power [W]	250–300
	Exposure time [μs]	20-40-60-80
Fixed parameters	Scanning strategy	Meander
	Hatch distance [μm]	90
	Point distance [μm]	90
	Laser spot size [μm]	65
	Atmosphere	Ar
	Thickness layer [μm]	30
	Platform temperature [°C]	30

(a)

(b)

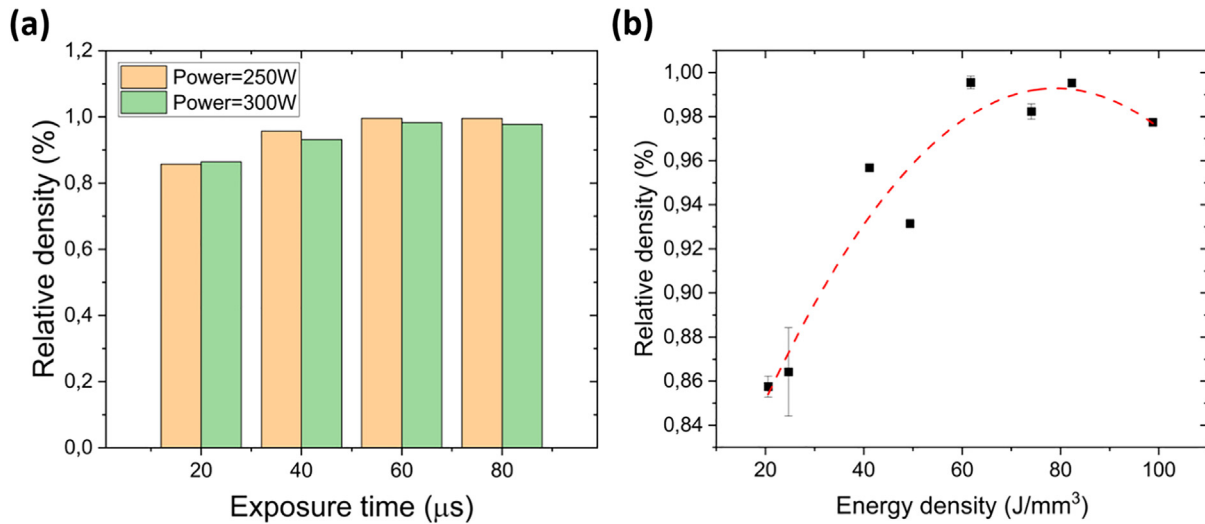**Fig. 2.** Evolution of the relative density as function of the investigated parameters, namely power and exposure time, (a) and of energy density Ψ (b).
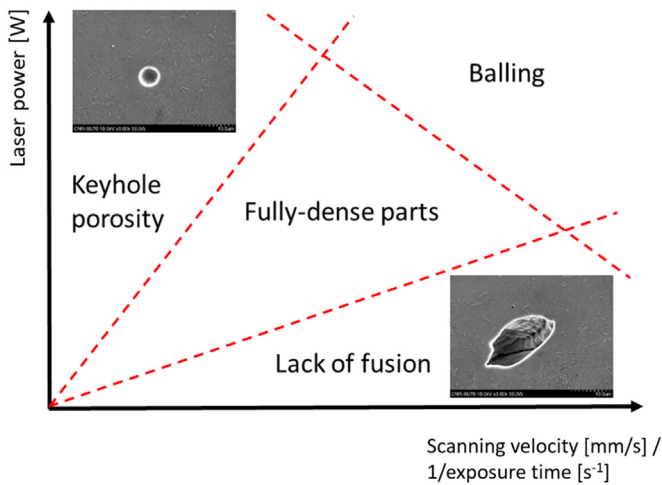

Fig. 3. Schematic of the feasibility area as function of the investigated process parameters. The principal defects are also highlighted in correspondence of the process parameters.

decay, depending on an excess of heat transferred to the liquid pools, which produces a limited vaporization of some material. This vaporized material can be entrapped in the liquid pool during its rapid solidification, therefore giving rise to small and spherical pores.

In the middle of the defects-containing regions of Fig. 3, an almost defect-free region, in which full dense parts can be achieved by the selection of the proper energy, can be found [30].

It can be seen from Fig. 2b that an energy density of 82 J/mm^3, corresponding to the process condition ($P = 250$ W; $t_{exp} = 80$ µs), is needed by the alloy for its proper melting and consolidation: a relative density of 99.5% was achieved, which is significantly higher than experimental results obtained in other works with similar TiB$_2$ content [15]. The obtained value of energy density appears to be in good agreement with other works in literature, dealing with the SLM of Al based powders with TiB$_2$ reinforcements [31,32].

From a thermodynamic point of view, the absorbed energy density condition needs to excess the ideal energy required by the material to reach its complete melting, E, according to the following equation (Eq. (2)):

$$E = \rho \cdot \left\{ C_p \cdot [T_M - T_i] + L_M \right\} \tag{2}$$

where ρ is the density; C_p is the thermal capacity; T_M and T_i are the melting and initial temperatures, respectively, and L_M is the latent heat of melting [33].

The current melting point and the corresponding latent heat of melting of the alloy under investigation were determined by DTA analysis, as depicted in Fig. 5. The melting temperature interval of the powder is quite large and the melting point is high, if compared to the ones of other SLMed aluminum alloys, such as the ones based on eutectic Al-Si
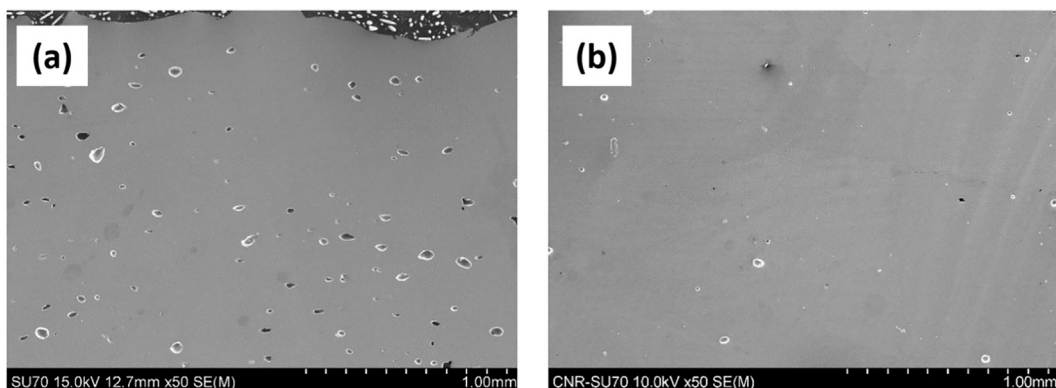

(a)

(b)

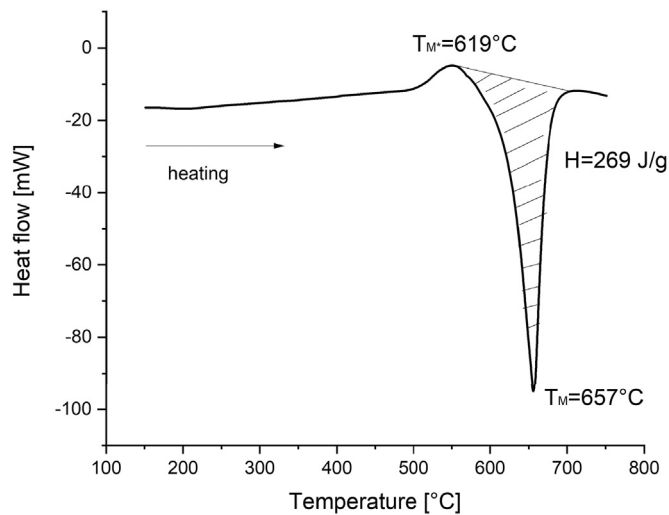**Fig. 4.** SEM images of the samples, produced at 42 J/mm^3 (a) and 82 J/mm^3 (b).

Fig. 5. DTA scan of the AlCu- TiB$_2$ powder.

system (AlSi10Mg, for instance), due to the limited amount of silicon in the alloy. In fact, melting takes place between 619 °C and 711 °C, with the peak lying at 657 °C, while the measured latent heat of melting was 269 J/g.

Considering a thermal capacity of 0.9 J/gK and an ideal powder packing coefficient of 0.6 [34], the ideal energy required for melting the alloy, E, can be calculated as equal to 1.4 J/mm^3. This value is in good agreement with theoretical values of energy density for the complete melting of metals carried out with the thermodynamic approach [26,35].

The absorbed energy density, calculated as Ψ multiplied by the absorption coefficient for an aluminum powder bed subjected to melting (in this case, it was assumed equal to 0.5 [36]), is 41 J/mm^3. Therefore, it can be affirmed that the absorbed energy density, experimentally identified from the peak of the relative density curve (see Fig. 2b), exceeds the ideal value of E.

The large difference between Ψ and E can be explained by several considerations, including the following: (i) overheating of the liquid pool is not considered; (ii) the contribution of the TiB$_2$ reinforcement is considered negligible; (iii) all the thermo-physical properties are considered temperature constant; (iv) energetic losses due to convection

and heat dissipation occurring during heat conduction are not considered. Moreover, literature indicates that multi-reflection of the laser beam occurs in the region of fully dense parts: the incident energy is absorbed and reflected between powder particles several times, therefore the energy density can be amplified and results to be higher than the theoretically needed energy [26]. It could be mentioned that the TiB$_2$ reinforcement should not remain in solid state under the effect of the laser scan: the maximum temperature during the melting is sufficient to go over the melting point of the AlCu alloy, but reasonably not high enough to melt TiB$_2$ (melting point of 3215 °C), as also suggested by other works in literature [31].

CT scan was carried out for confirming the measured density, resulting in a 99,66% relative density. Moreover, a deeper analysis of the observed defects was allowed by the CT analysis. Fig. 6 a shows the CT scan of the entire specimen produced in the identified optimal process condition, while representative vertical (namely xz) and horizontal (namely xy) sections are depicted in Fig. 6b, c, respectively. The detected defects are uniformly distributed across the entire volume with no evident clustering of the defects either in the core or along the borders of the sample. No evidence of the localization of defects along preferential directions, such as laser scans, could be found.

In Fig. 7 the quantitative analysis of the detected defects is reported; in particular, the defects size ranges approximately from 50 μm up to 350 μm, while only few defects can be as large as 500 μm. The sphericity of the defects varies between 0.3 and 0.8 (Fig. 7a). However, most of the defects, having size up to 200 μm, can be detected in a confined area, as shown in the plot shown in Fig. 7b. Analyzing both the graphs reported in Fig. 7, it can be concluded that the most frequent defects are spherical ones with a size below 100 μm. This analysis confirms the proper selection of the optimal process condition at an energy density of 82 J/mm^3, since it allowed to obtain high density and a favourablefavorable shape of the present defects, which are on average characterized by small size and high sphericity.

These results can be compared with the defects analysis performed with the same method by the authors [27] on an AlSi9Cu3 alloy, processed using the same SLM equipment; the size of defects was found to lie in a similar range.

3.2. Microstructural characterization

Fig. 8 shows the optical micrographs of sections lying orthogonal (indicated as xz plane; Fig. 8a) and parallel (indicated as xy plane;
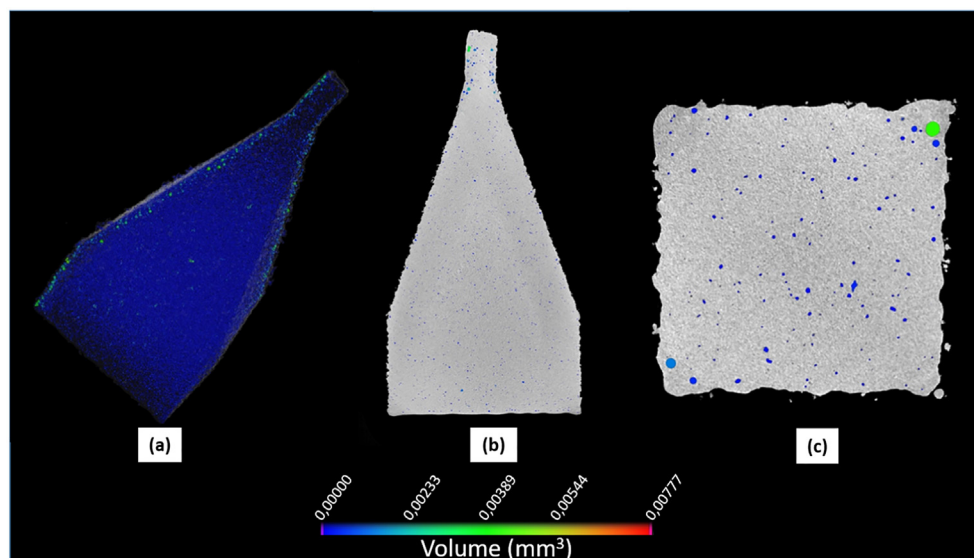

Fig. 6. 3D specimen reconstruction via CT (a); xz (b) and xy (c) views for defects analysis.
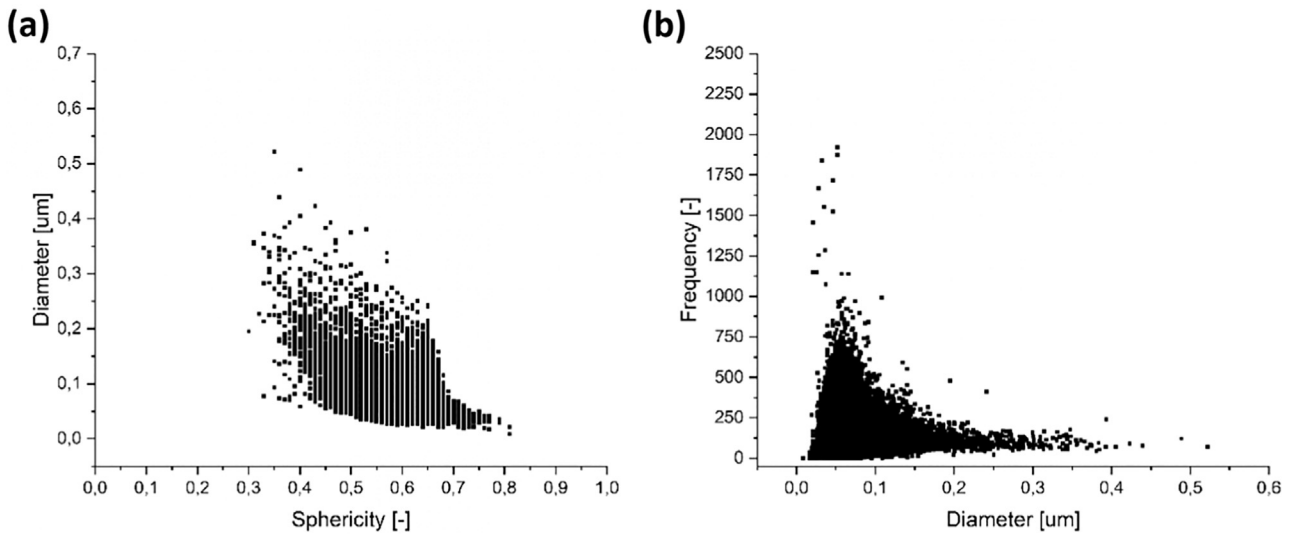
Fig. 7. Analysis of defects by CT scan: diameter - sphericity (a) and frequency - diameter (b) trends.

Fig. 8b) to the building platform. The typical layer by layer building strategy can be recognized, according with the presence of semi-elliptical liquid pools overlapped to each other. The detected shape of the liquid pools, which are approximately 120 μm in width and 90 μm in depth, is representative of the conduction mode welding, performed under irradiance, or density of power, below 10^5 W/cm^2 [27]. In fact, the aspect ratio of the liquid pool (width to depth ratio) is higher than 1, indicating that the principal active mechanism is complete melting of the alloy, without any significant vaporization under the effect of the laser beam. Therefore, it can be confirmed that the selected process condition (i.e. 82 J/mm^3) does not induce keyhole, which can be obtained under an irradiance higher than 10^6–10^7 W/cm^2.

XRD analysis performed on as-built sample is shown in Fig. 9: the spectrum shows the presence of two secondary phases, i.e. Al$_2$Cu (body-centered tetragonal, BCT) and TiB$_2$ (hexagonal close packed, HCP), in addition to the peaks related to the α-Al matrix. Relative height of the peaks of the latter phase are consistent with standard intensities from pure aluminum powder spectrum, suggesting the absence of preferred solidification texture.

The SEM observations were performed on as-built samples along xz plane, as shown in Fig. 10a, b, c. The grains can be easily distinguished in Fig. 10b thanks to the Cu segregation at the grain boundaries: they appear equiaxed and rather small. Melt pool boundaries, highlighted by dashed lines in Fig. 10b, c, d, are evidenced by grain growth in the heat-affected regions: the average grain size inside the melt pool is

about 0.5 μm, whilst it grows up to 2 μm at the melt pool boundaries. The microstructure revealed a homogeneous dispersion of TiB$_2$, visible as white spots in SE micrographs (comparable to EDS map of Fig. 10e), that were present both as single particle (see Fig. 10b, bottom) or few particle groups (Fig. 10b, upper left side). No direct correlation between the position of TiB$_2$ particles and the melt pool boundaries could be argued, even if grouped particles appear more frequently in their vicinity. Possibly, the dispersion of TiB$_2$ in the center of the melt pool is favoured by strong stirring experienced by the liquid metal heated by the laser in conduction mode [27], and no big agglomerates of particles were observed, contrarily to what found by Gao et al. [12]. The EBSD/EDX analyses not only confirmed the grain size and the presence of TiB$_2$ dispersed in Al matrix, but also showed no columnar texture nor epitaxial growth near the melt pool boundaries, which was also demonstrated by orientation imaging map (OIM) of aluminum matrix (Fig. 10d).

This result is quite different from the typical grain shape and size distribution in the more widespread SLMed Al-Si based alloys: AlSi10Mg, for example, usually exhibits columnar grain growth when produced using in both pulsed and continuous wave laser emission mode [22]. This feature of the AlCu-TiB$_2$ alloy is hindered by the presence of submicrometric particles, which can act as nucleation sites limiting grain growth, making the equiaxed microstructure more favorable. In fact, a well-known method of controlling grain size lies in promoting heterogeneous nucleation of an equiaxed structure by using in situ nucleating agents. The use of heterogeneous particles (e.g. TiB$_2$ in Al

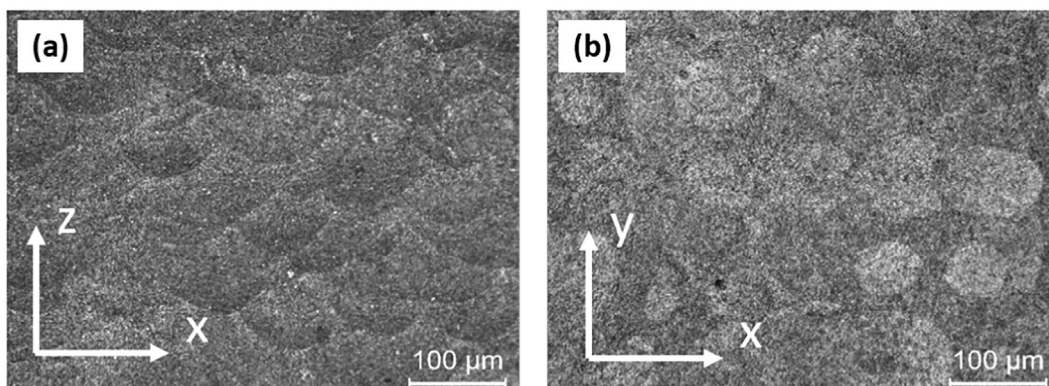**Fig. 8.** OM views of the xz (a) and xy (b) planes of the sample, built with 82 J/mm^2.
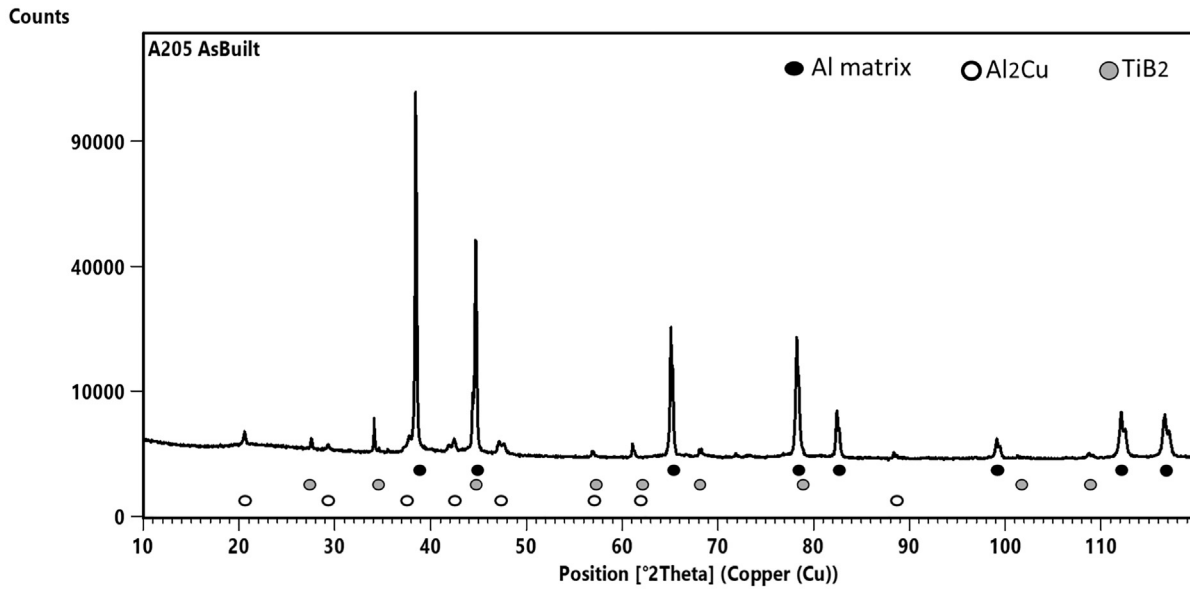
Fig. 9. XRD spectrum of the as-built specimen.

alloys) that can stimulate the nucleation of new grains in liquid melts, is a common practice in foundries aimed at refining the cast structure. It is well established that hot tearing resistance can be improved simultaneously, especially when nanoparticles are added to the cast melt [32,37] or inserted into the powder feedstock in AM [31,38,39].

TEM analyses, coupled with EDX mapping, confirmed the general features observed in the SEM: namely, grain size variation across the melt pool boundary, and also allowed the detection of other features of the microstructure. TiB_2 was found as both nanometric (Fig. 11) and micrometric elongated particles. It can be observed that Cu is distributed not only at the grain boundaries, where it reaches the Al_2Cu composition and structure, but also within the aluminum matrix, both as a dissolved element and in spherical particles containing Cu, Mg and Ag atoms. Other alloying elements, such as Ti, Mg and oxygen,

have been found to occasionally accumulate in such particles. In addition, Cu has been detected in spherical particles of complex composition with sizes smaller than 50 nm, which appear to have formed around central MgO-rich cores and nanopores; such particles have a mixed structure formed by multiple phases, as shown on the HAADF micrograph (Fig. 11c) and EDX maps (Fig. 11e): a detailed description of such particles is beyond the purpose of the present work. Ag, on the other hand, segregated preferentially at the interfaces of Cu-rich regions and TiB_2 particles with the matrix and at grain boundaries.

3.3. Mechanical characterization

The mechanical behaviour of the considered alloy was characterized under tensile conditions, as reported in Fig. 12. Yield strength, ultimate
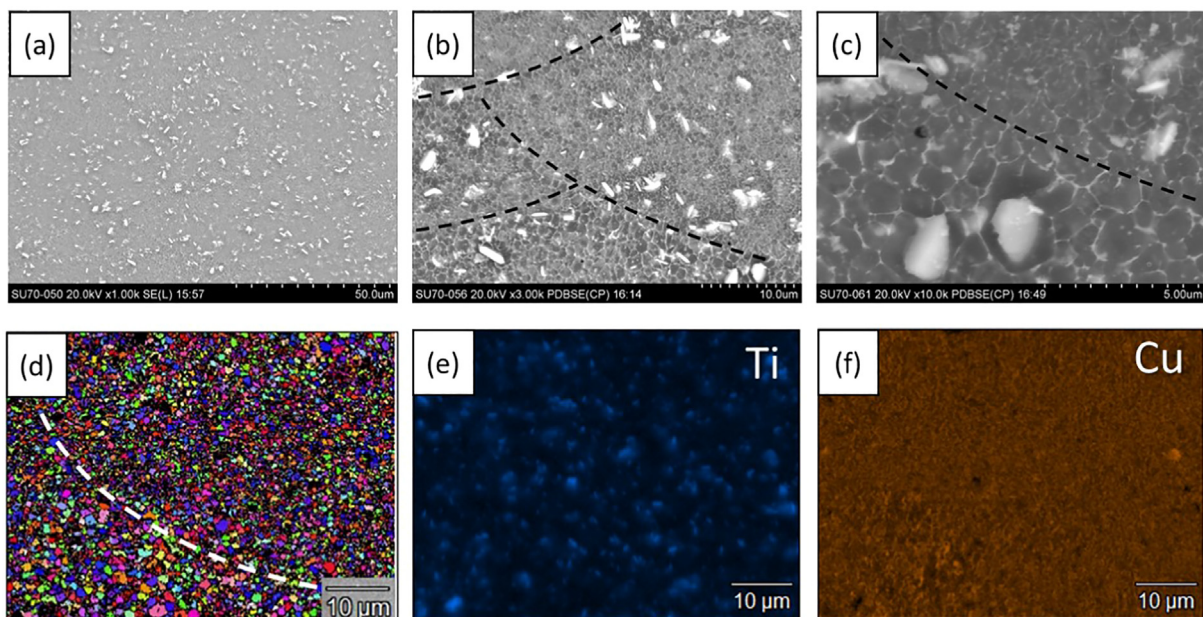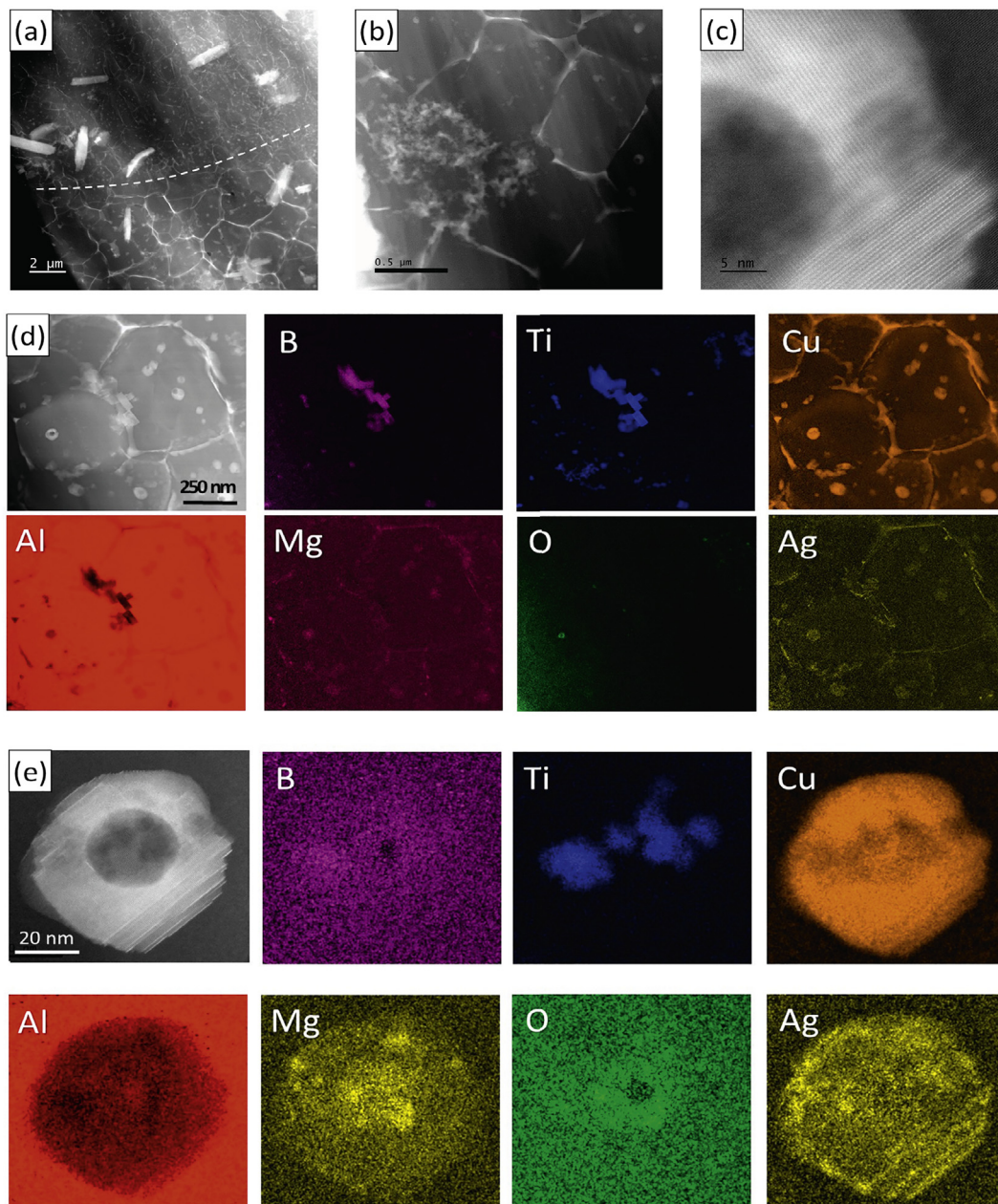

Fig. 10. SEM analyses on the as built material: a -b-c micrographs at different magnifications, b, c: black lines are drawn to help the individuation of melt pool boundaries, d-EBSD analyses results; OIM of the aluminum matrix in a region across a melt pool boundary (white dashed line) is shown, e, f - EDX maps of Ti, Cu acquired simultaneously to EBSD map.

Fig. 11. TEM micrographs showing a) a melt pool boundary region, b) cluster of nanometric TiB$_2$ particles, d) detail of rounded nanoparticle, and EDX maps performed on as built specimen, to assess d) element distribution and e) nanometric phases composition.

tensile strength and elongation to failure were found to be 317.8 ± 9.3 MPa, 391 ± 7.3 MPa and 12.5 ± 0.8%, respectively. It is immediately evident that the stress – strain curve presents an upper yield point, followed by a plateau ranging from yielding up to about 3% in strain. A similar behaviour was described in SLMed Al-Sc alloys and related to the formation of Luders bands in the very early stages of plastic deformation [40]. Moreover, the curve is characterized by the presence of discontinuities in the plastic flow, commonly related to the Portevin - Le Chatelier effect, similar to the ones reported by P. Mair et al. [41]. This latter macroscopic feature is connected on a microstructural level to the dynamic strain ageing (DSA) phenomenon. In literature different types of jerky flows are catalogued [42]: accordingly, type C serrations, visible as stress drops below the main level of the curve, seem to populate the initial yielding plateau. Thereafter, type A serrations (abrupt stress growths followed by a drop below the general level) characterize the initial part of the work hardening stage (between 3% and 4,5%

engineering strain); finally, type A serrations develop into type E ones (similar to the previous ones, but with little or no strain hardening) at larger plastic strain [43]. In order to better understand the mechanical behaviour of the present alloy, the strain hardening parameter Θ, also called work hardening parameter, was computed as $\Theta = \frac{d\sigma}{d\varepsilon}$, where σ and ε are true stress and true strain, respectively. The resulting evolution of Θ as function of true strain is plotted in Fig. 12b. It may be appreciated that, apart from the typical Θ decrease immediately after yielding, three stages can be roughly recognized. At low plastic strain, very low values of strain hardening correspond to the initial stress plateau; thereafter, an increase in strain hardening above 2000 MPa takes place; finally, Θ decreases more or less smoothly until Considère's criterion is reached (i.e. Θ and σ curves meet), indicating that uniform elongation and necking are attained before final failure.

Comparing the shape of the stress strain curve with the results of other alloys [22], and taking into consideration the relatively low
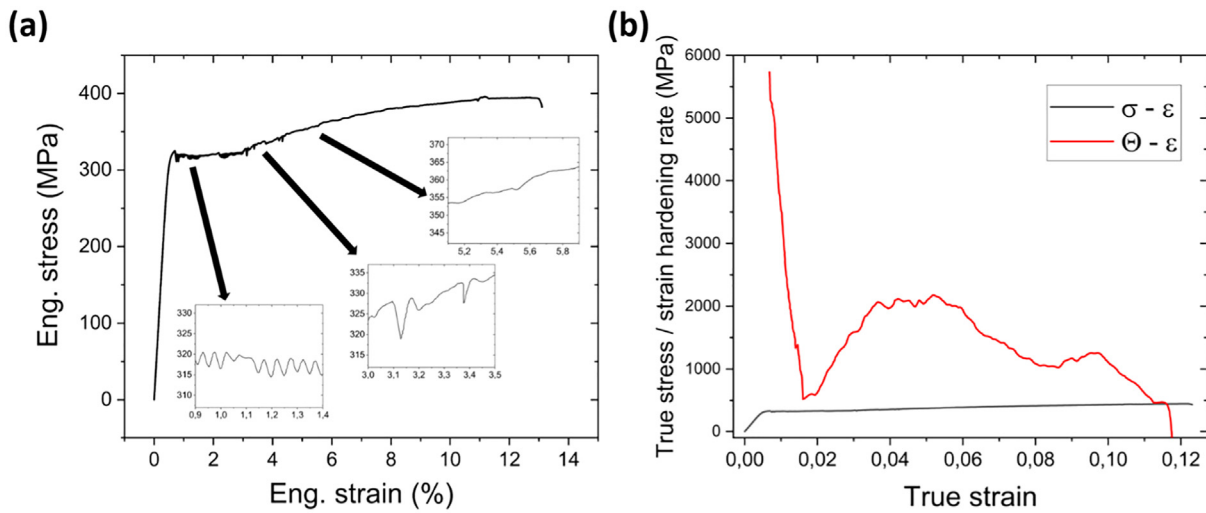
Fig. 12. (a) Engineering stress-strain curve; (b) true stress-strain curve, σ, and strain hardening rate, Θ, of the SLMed samples in the as-built condition.

work hardening exhibited by the alloy, it can be argued that the observed stress-strain curve shape is the consequence of the interaction of the dislocation with the high solute content in aluminum matrix. During cooling, the dislocations necessarily formed due to cooling stresses and thermal coefficient mismatch can be stabilized by the high solute content in the aluminum matrix: as indicated in TEM analyses, Cu is widely distributed in the matrix and forms few atomic clusters, which can be advantageous as pinning points for partial dislocations in FCC crystals. Consequently, an increased stress is necessary for the first movement of such dislocations (upper yield point). Thereafter, gliding dislocations are likely to encounter opposition to movement under the form of Cottrell atmospheres formed by the largely available solute atoms (reasonably copper atoms), which repeatedly lock and unlock them giving rise to C type serrations. During this stage the generation of new dislocations (and hence the strain hardening) is likely limited because of the rarity of strong pinning obstacles inside grains. After this initial stage, work hardening will increase as the results of further movement of dislocations, reaching grain boundaries and other

obstacles in the matrix (such as nanometric TiB_2 and Al_2Cu particles, grain and subgrain boundaries), which can bolster the generation of new dislocations and the dislocation forest pinning effect. Correspondingly a progressive reduction of serrations' frequency and a shift in their kind from type C to type A ones are observed, possibly because of the longer waiting times experienced by dislocations at available obstacles. Finally, pinning effect on dislocation will become less evident due to increased complexity of dislocation patterns, and, correspondingly, a decrease of strain hardening towards typical values of plastic flow is observed. The computed work hardening values are in the range of the ones typical of conventionally produced aluminum alloys or heat treated SLMed alloys, whereas they appear to be largely smaller than the ones displayed by as-built SLMed Si-bearing alloys, such as AlSi10Mg [44] or AlSi9Cu3 [27]. This overall smaller work hardening ability may be ascribed to the absence of hard phases arranged in an aligned fashion, such as the Si network composing cellular boundaries in SLMed Al-Si alloys, which were shown to generate numerous Orowan loops upon deformation [45].
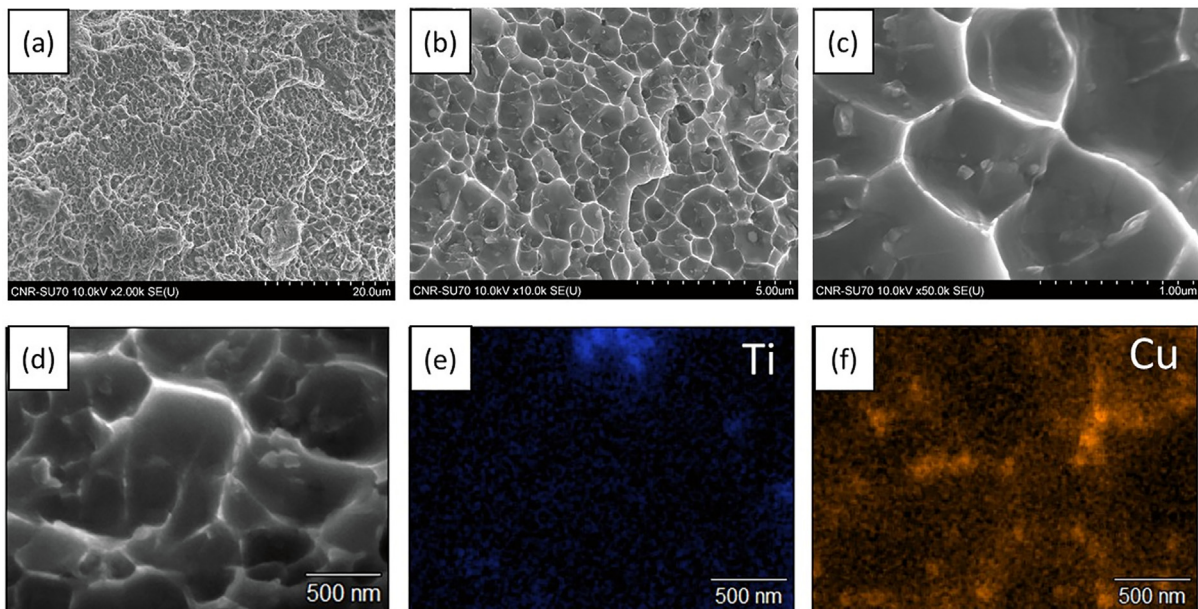

Fig. 13. Micrographs of fracture surfaces: a, b, c) secondary electron micrographs; d, e, f) EDS reference image and EDS maps of Ti and Cu of the fractured surface, respectively.

Micrographs of a representative fracture surface, as well as EDS analyses performed on it, are reported in Fig. 13. The fracture plane lies at approximately 45° with respect to the loading direction, in the plane of the maximum shear stresses, typical of highly ductile materials. Indeed, the appearance of the fracture surface observed at high magnification, is ductile, with dimples approximately of the same size of grains. Apparently no direct correlation between dimples boundaries and grain boundaries can be inferred; tiny, nanometric hints of fragile surfaces or cleavage were observed at the boundaries of the dimples, where higher concentration of Cu is present and eventually also the clusters of nanometric TiB_2 particles, observed with TEM analyses (Fig. 11b), causing a less smooth dethatching boundary, and possibly a reduction in ductility. At higher magnification, the Ti-rich (TiB_2) and Cu-rich particles that were observed in cross sections by SEM (Fig. 10) and TEM (Fig. 11a) were also found: they emerged partially from the dimple surface as highlighted by EDS mapping. They were present both at dimple bottoms and at dimple sides; possibly, they can contribute in dimples nucleation. Besides the overall ductile behaviour of the matrix, the total elongation to failure was rather limited: this aspect can be related to the presence of pores, acting as stress intensifiers, and to the presence of clusters of particles and Cu segregation at grain boundaries, that limit dimples coalescence. Likely, mechanical properties could be further improved by increasing density and implementing thermal treatments.

4. Conclusions

The following conclusions can be drawn:

- Process optimization allowed to obtain dense and sound SLMed parts. A consistent processing window characterized by limited defects was identified.
- The resulting microstructure is characterized by equiaxed and rather uniform grains. SLM process fast cooling rates together with stirring in the melt pool, promote engulfing rather than pushing of the already present TiB_2 reinforcing particles.
- The matrix is characterisedcharacterized by a relatively homogeneous distribution of solute Cu and Ag. Nevertheless, higher concentration of Cu, Ag and Mg were observed to enrich grain boundaries and interfaces with reinforcing particles. Small nanosized round particles of complex composition were observed in the matrix, denoting high potential for further increase of mechanical properties through aging treatments.
- The tensile behaviour displays an upper yielding point and jerky flow; a tentative correlation between such mechanical response and the observed microstructural features was proposed.

Data availability

The raw/processed data required to reproduce these findings cannot be shared at this time as the data also forms part of an ongoing study.

Declaration of Competing Interest

The authors declare that they have no known competing financial interests or personal relationships that could have appeared to influence the work reported in this paper.

Acknowledgements

References

[1] D. Herzog, V. Seyda, E. Wycisk, C. Emmelmann, Additive manufacturing of metals, Acta Mater. 117 (2016) 371–392, https://doi.org/10.1016/j.actamat.2016.07.019.

[2] E.O. Olakanmi, R.F. Cochrane, K.W. Dalgarno, A review on selective laser sintering/melting (SLS/SLM) of aluminium alloy powders: Processing, microstructure, and properties, J. Prog. Mater. Sci. 74 (2015) 401–477, https://doi.org/10.1016/j.pmatsci.2015.03.002.

[3] J. Zhang, B. Song, Q. Wei, D. Bourell, Y. Shi, A review of selective laser melting of aluminum alloys: processing, microstructure, property and developing trends, J. Mater. Sci. Technol. 35 (2019) 270–284, https://doi.org/10.1016/j.jmst.2018.09.004.

[4] M. Di Sabatino, L. Arnberg, Castability of aluminium alloys, Trans. Indian Inst. Metals 62 (2009) 321–325, https://doi.org/10.1007/s12666-009-0049-2.

[5] H. Zhang, H. Zhu, T. Qi, Z. Hu, X. Zeng, Selective laser melting of high strength Al – Cu – Mg alloys: Processing, microstructure and mechanical properties, Mater. Sci. Eng. A 656 (2016) 47–54, https://doi.org/10.1016/j.msea.2015.12.101.

[6] X. Nie, H. Zhang, H. Zhu, Z. Hu, L. Ke, X. Zeng, Analysis of processing parameters and characteristics of selective laser melted high strength Al-Cu-Mg alloys: from single tracks to cubic samples, J. Mater. Process. Technol. 256 (2018) 69–77, https://doi.org/10.1016/j.jmatprotec.2018.01.030.

[7] A. Aversa, G. Marchese, A. Saboori, E. Bassini, D. Manfredi, S. Biamino, D. Ugues, P. Fino, M. Lombardi, New aluminum alloys specifically designed for laser powder bed fusion: A review, Materials (Basel) 12 (2019) https://doi.org/10.3390/ma12071007.

[8] M. Albu, R. Krisper, J. Lammer, G. Kothleitner, J. Fiocchi, P. Bassani, Microstructure Evolution during In-Situ Heating of AlSi10Mg Alloy Powders and Additive Manufactured Parts, 2020 https://doi.org/10.1016/j.addma.2020.101605.

[9] L. Hitzler, S. Hafenstein, F. Mendez Martin, H. Clemens, E. Sert, A. Öchsner, M. Merkel, E. Werner, Heat treatments and critical quenching rates in additively manufactured Al–Si–Mg alloys, Materials 13 (2020) 720, https://doi.org/10.3390/ma13030720.

[10] R. Casati, M. Coduri, M. Riccio, A. Rizzi, M. Vedani, Development of a high strength Al–Zn–Si–Mg–Cu alloy for selective laser melting, J. Alloys Compd. 801 (2019) 243–253, https://doi.org/10.1016/j.jallcom.2019.06.123.

[11] J.H. Martin, B.D. Yahata, J.M. Hundley, J.A. Mayer, T.A. Schaedler, T.M. Pollock, 3D printing of high-strength aluminium alloys, Nat. Publ. Gr. (2017) https://doi.org/10.1038/nature23894.

[12] C. Gao, Z. Wang, Z. Xiao, D. You, K. Wong, A.H. Akbarzadeh, Selective laser melting of TiN nanoparticle-reinforced AlSi10Mg composite: microstructural, interfacial, and mechanical poperties, J. Mater. Process. Technol. 281 (2020) 116618, https://doi.org/10.1016/j.jmatprotec.2020.116618.

[13] H. Zhang, H. Zhu, X. Nie, J. Yin, Z. Hu, X. Zeng, Effect of zirconium addition on crack, microstructure and mechanical behavior of selective laser melted Al-cu-mg alloy, Scr. Mater. 134 (2017) 6–10, https://doi.org/10.1016/j.scriptamat.2017.02.036.

[14] A.B. Spierings, K. Dawson, T. Heeling, P.J. Uggowitzer, R. Schäublin, F. Palm, K. Wegener, Microstructural features of Sc- and Zr-modi fi ed Al-Mg alloys processed by selective laser melting, JMADE. 115 (2017) 52–63, https://doi.org/10.1016/j.matdes.2016.11.040.

[15] P. Wang, C. Gammer, F. Brenne, T. Niendorf, J. Eckert, S. Scudino, A heat treatable TiB_2/Al-3.5Cu-1.5Mg-1Si composite fabricated by selective laser melting: Microstructure, heat treatment and mechanical properties, Compos. Part B Eng. 147 (2018) 162–168, https://doi.org/10.1016/j.compositesb.2018.04.026.

[16] F. Belelli, R. Casati, M. Riccio, A. Rizzi, M.Y. Kayacan, M. Vedani, Development of a novel high-temperature Al alloy for laser powder bed fusion, Metals (Basel) 11 (2021) 125–170, https://doi.org/10.3390/met11010035.

[17] Y.J. Liu, Z. Liu, Y. Jiang, G.W. Wang, Y. Yang, L.C. Zhang, Gradient in microstructure and mechanical property of selective laser melted AlSi10Mg, J. Alloys Compd. 735 (2018) 1414–1421, https://doi.org/10.1016/j.jallcom.2017.11.020.

[18] https://www.cabiran.com/cwsd.php?Z3AuPTQ0MQ/NDA/ZWlmYm1rb3BjRWl-YHoicXd1.pdf.

[19] https://www.aeromet.co.uk/a20x.

[20] L. Xi, D. Gu, S. Guo, R. Wang, K. Ding, K.G. Prashanth, Grain refinement in laser manufactured Al-based composites with TiB_2 ceramic, J. Mater. Res. Technol. 9-3 (2020) 2611–2622.

[21] J. Fiocchi, A. Tuissi, P. Bassani, C.A. Biffi, Low temperature annealing dedicated to AlSi10Mg selective laser melting products, J. Alloys Compd. 695 (2017) 3402–3409, https://doi.org/10.1016/j.jallcom.2016.12.019.

[22] C.A. Biffi, J. Fiocchi, P. Bassani, A. Tuissi, Continuous wave vs pulsed wave laser emission in selective laser melting of AlSi10Mg parts with industrial optimized process parameters: microstructure and mechanical behaviour, Addit. Manuf. 24 (2018) 639–646, https://doi.org/10.1016/j.addma.2018.10.021.

[23] R.K. Won, B.B. Gyung, H.P. Jung, W.L. Taeg, L. Byoung-Soo, Y. Seung-Min, K. Gun-Hee, L. Kwangchoon, G.K. Hyung, Microstructural study on a Fe-10Cu alloy fabricated by selective laser melting for defect-free process optimization based on the energy density, J. Mater. Res. Technol. 9 (6) (2020) 12834–12839, https://doi.org/10.1016/j.jmrt.2020.09.051.

[24] J.P. Oliveira, A.D. Lalonde, J. Ma, Processing parameters in laser powder bed fusion metal additive manufacturing, Mater. Des. 193 (2020) 108762.

[25] B. Zhang, Y. Li, Q. Bai, Defect formation mechanisms in selective laser melting: a review, Chin. J. Mech. Eng. 30 (2017) 515–527, https://doi.org/10.1007/s10033-017-0121-5.

[26] Wayne E. King, Holly D. Barth, Victor M. Castillo, Gilbert F. Gallegos, John W. Gibbs, Douglas E. Hahn, Chandrika Kamath, Alexander M. Rubenchik, Observation of keyhole-mode laser melting in laser powder-bed fusion additive manufacturing, J. Mater. Process. Technol. 214 (12) (2014) 2915–2925, https://doi.org/10.1016/j.jmatprotec.2014.06.005.

[27] J. Fiocchi, C.A. Biffi, A. Tuissi, Selective laser melting of high-strength primary AlSi9Cu3 alloy: Processability, microstructure, and mechanical properties, Mater. Des. 191 (2019) 108581.

[28] C.A. Biffi, J. Fiocchi, Valenza F. Bassani, P. Tuissi, Selective laser melting of NiTi shape memory alloy: processability, microstructure, and superelasticity, Shape Mem. Superelastic. 6 (3) (2020) 342–353.

[29] C.A. Biffi, A.G. Demir, M. Coduri, B. Previtali, A. Tuissi, Laves phases in selective laser melted TiCr1.78 alloys for hydrogen storage, Mater. Lett. (2018)https://doi.org/10.1016/j.matlet.2018.05.028.

[30] Luke Johnson, Mohamad Mahmoudi, Bing Zhang, Raiyan Seede, Xueqin Huang, Janine T. Maier, Hans J. Maier, Ibrahim Karaman, Alaa Elwany, Raymundo Arróyave, Assessing printability maps in additive manufacturing of metal alloys, Acta Mater. 176 (2019) 199–210.

[31] S.Y. Zhou, Y. Su, H. Wang, J. Enz, T. Ebel, M. Yan, Selective laser melting additive manufacturing of 7xxx series Al-Zn-mg-cu alloy: cracking elimination by co-incorporation of Si and TiB_2, Addit. Manufact. 36 (2020) 101458.

[32] X.P. Li, G. Ji, Z. Chen, A. Addad, Y. Wu, H.W. Wang, J. Vleugels, J. Van Humbeeck, J.P. Kruth, Selective laser melting of nano-TiB_2 decorated AlSI10Mg alloy with high fracture strength and ductility, Acta Mater. 29 (2017) 183–193.

[33] LIA Handbook of Laser Materials Processing (Ed.), Editors: Editor-in-chief: Ready, John F. Farson, D.F., Feeley, T. (Eds.), 2001 , ISBN 978-3-540-41770-5.

[34] K.-H. Lee, G.J. Yun, A novel heat source model for analysis of melt pool evolution in selective laser melting process, Addit. Manufact. 36 (2020) 101497.

[35] Hyung Giun Kim, Won Rae Kim, Ohyung Kwon, Gyung Bae Bang, Min Ji Ham, Hyung-Ki Park, Kyung-Hwan Jung, Kang Min Kim, Chang-Woo Lee, Gun-Hee Kim, Laser beam melting process based on complete-melting energy density for commercially pure titanium, J. Manuf. Process. 45 (2019) 455–459 , ISSN 1526–6125 https://doi.org/10.1016/j.jmapro.2019.07.031.

[36] C.D. Boley, S.A. Khairallah, A.M. Rubenchik, Calculation of laser absorption by metal powders in additive manufacturing, Appl. Opt. 54-9 (2015) 2477–2482.

[37] H. Choi, W.-H. Cho, H. Konishi, S. Kou, X. Li, Nanoparticle-induced superior hot tearing resistance of A206 alloy, Metall. Mater. Trans. A 44A (2013) 1897–1907.

[38] X. Zhon, Z. An, Z. Shen, W. Liu, C. Yao, Particle control in selective laser melting in-situ oxide dispersion strengthened method, OP Conf. Ser. Mater Sci. Eng. 167 (2017), 012048, .

[39] P. Yuan, D. Gu, D. Dai, Particulate migration behavior and its mechanism durng selective laser melting of TiC reinforced Al matrix nanocomposites, Mater. Design 82 (2015) 46–55.

[40] Q. Jia, P. Rometsch, S. Cao, K. Zhang, X. Wu, Towards a high strength aluminium alloy development methodology for selective laser melting, Mater. Des. 174 (2019) 107775, https://doi.org/10.1016/j.matdes.2019.107775.

[41] P. Mair, L. Kaserer, J. Braun, N. Weinberger, I. Letofsky-Papst, G. Leichtfried, Microstructure and mechanical properties of a TiB_2-modified Al–cu alloy processed by laser powder-bed fusion, Mater. Sci. Eng. A 799 (2021)https://doi.org/10.1016/j.msea.2020.140209.

[42] A. Benallal, T. Berstad, T. Børvik, A.H. Clausen, O.S. Hopperstad, Dynamic strain aging and related instabilities: experimental, theoretical and numerical aspects, Eur. J. Mech. A Solids 25 (2006) 397–424, https://doi.org/10.1016/j.euromechsol.2005.10.007.

[43] P. Rodriguez, S. Venkadesan, Serrated plastic flow, Solid State Phenom. 42–43 (1995) 257–266, https://doi.org/10.4028/www.scientific.net/SSP.42-43.257.

[44] P. Ma, K.G. Prashanth, S. Scudino, Y. Jia, H. Wang, C. Zou, et al., Influence of annealing on mechanical properties of Al-20Si processed by selective laser melting, Metals (Basel) 4 (2014) 28–36, https://doi.org/10.3390/met4010028.

[45] B. Chen, S.K. Moon, X. Yao, G. Bi, J. Shen, J. Umeda, et al., Strength and strain hardening of a selective laser melted AlSi10Mg alloy, Scr. Mater. 141 (2017) 45–49, https://doi.org/10.1016/j.scriptamat.2017.07.025.